



# Direct evidence of surface exposed water ice in the lunar polar regions

Shuai Li<sup>a,b,1</sup>, Paul G. Lucey<sup>a</sup>, Ralph E. Milliken<sup>b</sup>, Paul O. Hayne<sup>c</sup>, Elizabeth Fisher<sup>b</sup>, Jean-Pierre Williams<sup>d</sup>, Dana M. Hurley<sup>e</sup>, and Richard C. Elphic<sup>f</sup>

<sup>a</sup>Department of Geology and Geophysics, University of Hawaii, Honolulu, HI 96822; <sup>b</sup>Department of Earth, Environmental and Planetary Sciences, Brown University, Providence, RI 02912; <sup>c</sup>Department of Astrophysical & Planetary Sciences, University of Colorado Boulder, Boulder, CO 80309; <sup>d</sup>Department of Earth, Planetary, and Space Sciences, University of California, Los Angeles, CA 90095; <sup>e</sup>Applied Physics Laboratory, Johns Hopkins University, Laurel, MD 20723; and <sup>f</sup>Ames Research Center, NASA, Mountain View, CA 94035

Edited by Jonathan I. Lunine, Cornell University, Ithaca, NY, and approved July 20, 2018 (received for review February 8, 2018)

**Water ice may be allowed to accumulate in permanently shaded regions on airless bodies in the inner solar system such as Mercury, the Moon, and Ceres [Watson K, et al. (1961) *J Geophys Res* 66:3033–3045]. Unlike Mercury and Ceres, direct evidence for water ice exposed at the lunar surface has remained elusive. We utilize indirect lighting in regions of permanent shadow to report the detection of diagnostic near-infrared absorption features of water ice in reflectance spectra acquired by the Moon Mineralogy Mapper [M (3)] instrument. Several thousand M (3) pixels (~280 × 280 m) with signatures of water ice at the optical surface (depth of less than a few millimeters) are identified within 20° latitude of both poles, including locations where independent measurements have suggested that water ice may be present. Most ice locations detected in M (3) data also exhibit lunar orbiter laser altimeter reflectance values and Lyman Alpha Mapping Project instrument UV ratio values consistent with the presence of water ice and also exhibit annual maximum temperatures below 110 K. However, only ~3.5% of cold traps exhibit ice exposures. Spectral modeling shows that some ice-bearing pixels may contain ~30 wt % ice that is intimately mixed with dry regolith. The patchy distribution and low abundance of lunar surface-exposed water ice might be associated with the true polar wander and impact gardening. The observation of spectral features of H<sub>2</sub>O confirms that water ice is trapped and accumulates in permanently shadowed regions of the Moon, and in some locations, it is exposed at the modern optical surface.**

lunar polar regions | permanently shaded regions | lunar water ice | near-infrared spectroscopy | Moon mineralogy mapper

The small tilt of the rotation axes of Mercury, the Moon, and Ceres with respect to the ecliptic causes topographic depressions in their polar regions, such as impact craters, to be permanently shadowed from sunlight (1). As a consequence, surface temperatures in these regions are extremely low (i.e., less than 110 K) (1–3) and are limited only by heat flow from the interior and sunlight reflected from adjacent topography (4–6). These areas are predicted to act as cold traps that are capable of accumulating volatile compounds over time, supported by observations of water ice at the optical surface of polar shadowed locations on Mercury (7–9) and Ceres (10, 11). There are a number of strong indications of the presence of water ice in similar cold traps at the lunar poles (12–14), but none are unambiguously diagnostic of surface-exposed water ice, and inferred locations of water ice from different methods are not always correlated. Epithermal neutron counts, for instance, can be used to estimate hydrogen in the upper tens of centimeters of the lunar regolith, but such data cannot isolate the uppermost (e.g., optical) surface and cannot discriminate between H<sub>2</sub>O, OH, or H (14). Ratios of reflected UV radiation measured by the Lyman Alpha Mapping Project (LAMP) instrument onboard the Lunar Reconnaissance Orbiter (LRO) have been interpreted to indicate the presence of H<sub>2</sub>O near the lunar south pole (13), but the observed signatures may not be uniquely attributable to

water ice because OH may exhibit similar characteristics at UV wavelengths (15). High reflectance values at 1,064-nm wavelength have also been observed near the lunar poles by the Lunar Orbiter Laser Altimeter (LOLA) and may be consistent with water ice, but fine particles and lunar regolith with lower degrees of space weathering may also give rise to higher reflectivity at this wavelength, making this interpretation nonunique (12, 16).

An advantage of near-infrared (NIR) reflectance spectroscopy is that it provides a direct measurement of molecular vibrations and can thus be used to discriminate H<sub>2</sub>O ice from OH and H<sub>2</sub>O in other forms (e.g., liquid, surface adsorbed, or bound in minerals). NIR reflectance data acquired by the Moon Mineralogy Mapper [M (3)] instrument on the Chandrayaan-1 spacecraft provide the highest spatial and spectral resolution NIR data currently available at a global scale, including the polar regions. The wavelength range of M (3) (0.46–2.98 μm) is too limited to properly discriminate OH/H<sub>2</sub>O species using fundamental vibration modes in the 3-μm region (17, 18), and in this study we focus on the detection of diagnostic overtone and combination mode vibrations for H<sub>2</sub>O ice that occur near 1.3, 1.5, and 2.0 μm. Numerical modeling results suggest NIR spectra representing as little as 5 wt % (intimate mixing) or 2 vol % (linear areal mixing) water ice are expected to exhibit all three of these absorptions (*Methods* and *SI Appendix, Fig. S1*), although actual detection limits in the M (3) data are dependent on instrumental response and signal-to-noise ratios (SNR).

The cooccurrence of all three absorptions would be evidence for water ice, and M (3) data (optical period 2C) at high latitudes were searched for pixels in shadow whose spectra exhibited these features (*Methods* and *SI Appendix, Table S1*). The resulting subset of pixels (spectra) was then analyzed using the spectral

## Significance

**We found direct and definitive evidence for surface-exposed water ice in the lunar polar regions. The abundance and distribution of ice on the Moon are distinct from those on other airless bodies in the inner solar system such as Mercury and Ceres, which may be associated with the unique formation and evolution process of our Moon. These ice deposits might be utilized as an in situ resource in future exploration of the Moon.**

Author contributions: S.L. designed research; S.L. performed research; S.L. contributed new reagents/analytic tools; S.L., P.G.L., R.E.M., P.O.H., E.F., J.-P.W., D.M.H., and R.C.E. analyzed data; and S.L., P.G.L., and R.E.M. wrote the paper.

The authors declare no conflict of interest.

This article is a PNAS Direct Submission.

This open access article is distributed under [Creative Commons Attribution-NonCommercial-NoDerivatives License 4.0 \(CC BY-NC-ND\)](https://creativecommons.org/licenses/by-nc-nd/4.0/).

<sup>1</sup>To whom correspondence should be addressed. Email: shuaili@hawaii.edu.

This article contains supporting information online at [www.pnas.org/lookup/suppl/doi:10.1073/pnas.1802345115/-DCSupplemental](https://www.pnas.org/lookup/suppl/doi:10.1073/pnas.1802345115/-DCSupplemental).

angle mapping method as a metric to assess the similarity of spectral slopes and absorption features between the M (3) spectra and a laboratory spectrum of pure water frost (*Methods*). This step relies on the fact that reflectance spectra of water ice exhibit strong “blue” spectral continuum slopes (reflectance decreases with increasing wavelength) (*SI Appendix, Fig. S1*), whereas typical lunar spectra exhibit an opposite “reddening” effect due to nanophase iron produced during space weathering (19). A spectral angle less than 30° between each M (3) spectrum and the water frost spectrum was empirically determined to define the final subset of M (3) pixels most consistent with the presence of water ice (*Methods*).

## Results and Discussion

Reflectance measurements in regions of permanent shadow are enabled by sunlight scattered off crater walls or other nearby topographic highs. The shaded regions studied here lie between directly illuminated areas and areas of deep permanent shadow, and the analysis was limited to pixels for which local solar incidence angle was greater than 90° to ensure the corresponding surface was in shadow. As expected for areas only receiving indirect illumination, the SNR of M (3) pixels in these locations is low, and we evaluated the possibility that our process was selecting noisy spectra that mimic ice spectra by random chance. A random dataset was generated that matched the means and SDs of M (3) data in shaded regions near the lunar poles (75° N/S–90° N/S), but with five times more pixels than M (3) data (~65 × 10<sup>6</sup> points). The same procedures were performed on the random dataset as on the original M (3) data to detect potential ice absorption features. Only 10<sup>-4</sup>% of those random points passed our detection criteria, which may indicate the rate of false-positive detections due to random noise. In contrast, ~0.2% of shaded M (3) data showed positive detections (*SI Appendix, Fig. S2C*). The average spectrum of positive detections of the random data (*SI Appendix, Fig. S3*) is distinct from those observed in the M (3) data (Fig. 1), indicating that a population of random noise of a size similar to that of the M (3) data is highly unlikely to produce ice-like spectra.

A null hypothesis test was conducted to show that the prediction of a third ice-like absorption based on detection of the other two is significant (*SI Appendix, Tables S2 and S3*). Water ice must exhibit all three absorptions, and a failure to detect all three casts doubt on its presence. When potential ice spectra were identified in the M (3) data based solely on the presence of two of the three NIR ice absorptions, the third ice-like absorption was always observed in the average spectra of the positive pixels (*SI Appendix, Fig. S4*). It is thus statistically significant to conclude that the three absorptions near 1.3, 1.5, and 2.0 μm occur simultaneously in a subset of the M (3) data, which is consistent with the presence of water ice in these pixels.

The latitudinal distribution of potential ice detections was used as further validation. All M (3) pixels over all latitudes that were locally shaded from the sun at the time of the observations were tested for the presence of the three water-ice absorptions (shaded surfaces were abundant near the equator when the spacecraft orbit was near the terminator). These data should exhibit similar instrument noise and systematic errors as polar surfaces in permanent shadow. At low latitudes these data include surfaces that experience high temperatures near local noon and thus could not support surface ice (i.e., they are not permanently shadowed). No positive detections at <70° latitude were observed: only pixels in shaded regions within 20° of each pole showed positive detections, and >90% of the detections were located at latitudes within 10° of the pole (*SI Appendix, Fig. S2*). M (3) spectra exhibiting the cooccurrence of three diagnostic water-ice bands are thus only observed in shadowed regions at high latitudes.

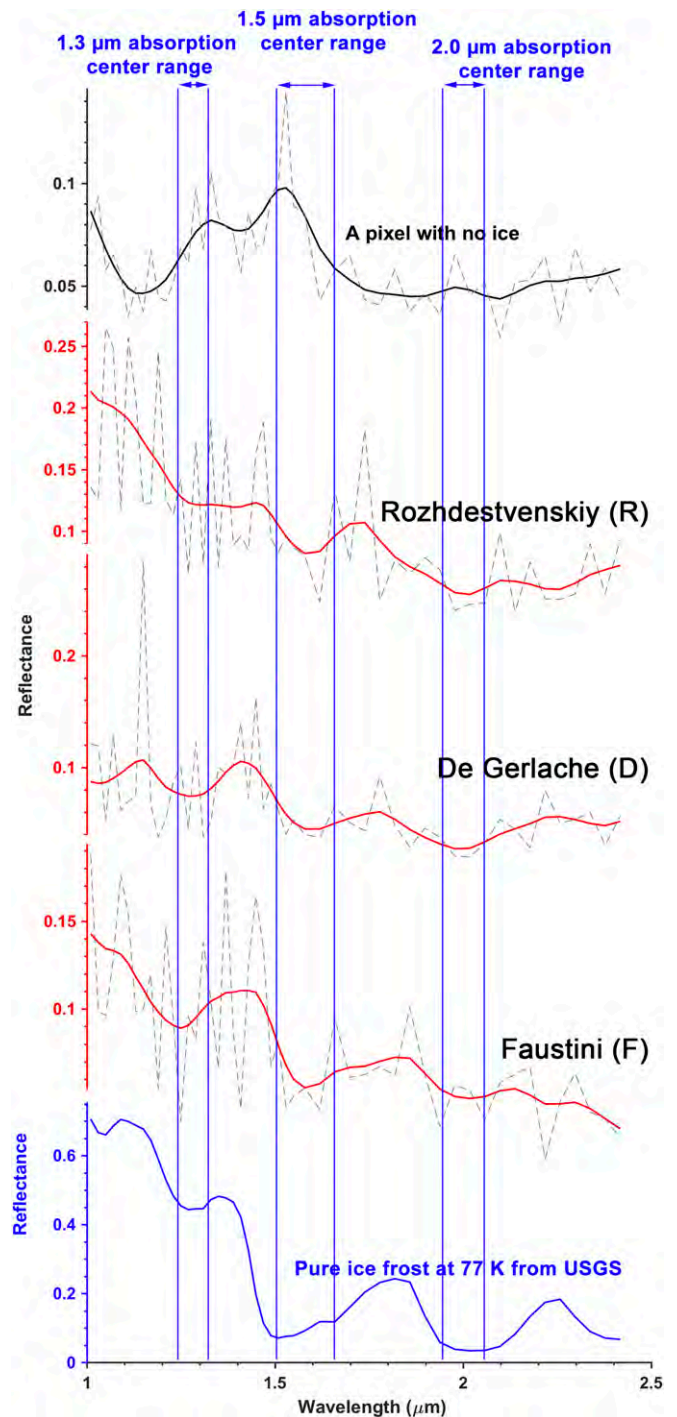


**Fig. 1.** Example M (3) reflectance spectra of ice-bearing pixels (red) and non-ice-bearing pixels (black) plotted with a laboratory spectrum of pure water ice (blue); solid lines are smoothed spectra based on a cubic spline algorithm (33).

Three example M (3) spectra are presented in Fig. 1 for possible ice-bearing pixels near the rim of crater Faustini, the crater De Gerlache in the south pole, and near the crater Rozhdestvenskiy in the north pole of the Moon (see yellow arrows in Fig. 4). The M (3) spectra of possible ice-bearing pixels are noisy due to the faint light source in the shaded regions, but absorption features near 1.3, 1.5, and 2.0 μm in these examples are all consistent with those of water ice, whereas similar features

are not observed in an example spectrum that did not pass the ice detection criteria (Fig. 1).

The spectra of all ice-bearing pixels were averaged and plotted for the northern (Fig. 2 *A* and *B*) and the southern (Fig. 2 *C* and *D*) polar regions to further reduce noise. The 1.5- $\mu\text{m}$  absorption appears broader and more asymmetric in the average spectrum for the south compared with that from the north (Fig. 2), which is suggestive of larger grain sizes in the former (20). Spectral mixing model results suggest that the weak absorption near 1.1  $\mu\text{m}$  and the blue slope of the M (3) spectra (Fig. 2) may be indicative of 30 wt % ice or higher if it is mixed intimately with regolith, or over 20 vol % if ice occurs as patches within otherwise ice-free regolith (*Methods* and *SI Appendix*, Fig. S1).

The absorption minima near 1.5  $\mu\text{m}$  of the M (3) spectra of ice-bearing pixels appear to be shifted  $\sim 0.05$   $\mu\text{m}$  to longer wavelengths compared with those of pure ice frost (Figs. 1 and 2). Such band shifts may reflect the increase of hydrogen bond strength due to water being bound with minerals (21). However, there was no apparent shift of the absorption near 1.5  $\mu\text{m}$  observed for olivine (1%) and water-ice (99%) mixtures (22), which may not represent the lunar case where the ice abundance may not be higher than 30%. Although there is no independent evidence to support such band shifts are due to molecular water bound to the surfaces of minerals that typify the lunar surface, such as pyroxene, plagioclase, olivine, ilmenite, and agglutinate, we cannot rule out the possibility that the apparent 0.05- $\mu\text{m}$  shift of the 1.5- $\mu\text{m}$  absorption represents water associated with certain hydrous minerals as some hydrous salts exhibit water bands close to  $\sim 1.55$   $\mu\text{m}$ . However, such minerals have not been observed in

returned lunar samples and most hydrous salts are unlikely to be stable under the vacuum and low-humidity conditions of the lunar surface.

Alternatively, previous studies found that the OH fundamental stretching vibration shifted from  $\sim 2.94$   $\mu\text{m}$  ( $\sim 3,400$   $\text{cm}^{-1}$ ) for high-density ice to  $\sim 3.09$   $\mu\text{m}$  ( $\sim 3,230$   $\text{cm}^{-1}$ ) for low-density ice that was condensed from a vapor phase (23). The overtone absorption in the case of the low-density ice would be expected to occur near  $\sim 1.55$   $\mu\text{m}$ . The apparent 0.05- $\mu\text{m}$  shift of  $\text{H}_2\text{O}$  absorptions in the M (3) spectra could thus be consistent with the presence of low-density ice condensed from a vapor phase, a process that would be consistent with water delivered by volatile-rich impactors or migration of water molecules through the lunar exosphere toward cold traps. However, we cannot fully rule out the possibility that the 0.05- $\mu\text{m}$  shift [a range of two M (3) spectral bands] of the 1.5- $\mu\text{m}$  absorptions is due to the low SNR of the M (3) data.

Potential ice-bearing regions identified in the M (3) data were compared with LOLA reflectance (12), LAMP UV ratio (13), and Diviner maximum annual temperature values (24) to provide an independent check on whether or not these locations are consistent with the presence of water ice at the optical surface. We found that 93.2% of the M-(3)-derived ice locations also exhibited extreme LOLA reflectance and UV ratio values consistent with the presence of water ice, as well as annual maximum surface temperatures below 110 K (Fig. 3). The small number of candidate locations with slightly higher surface temperatures (110–160 K) or lower LOLA reflectance values (0.3–0.32, where 0.32 is the mean value near both poles from  $75^\circ$  to  $90^\circ$ ) may be

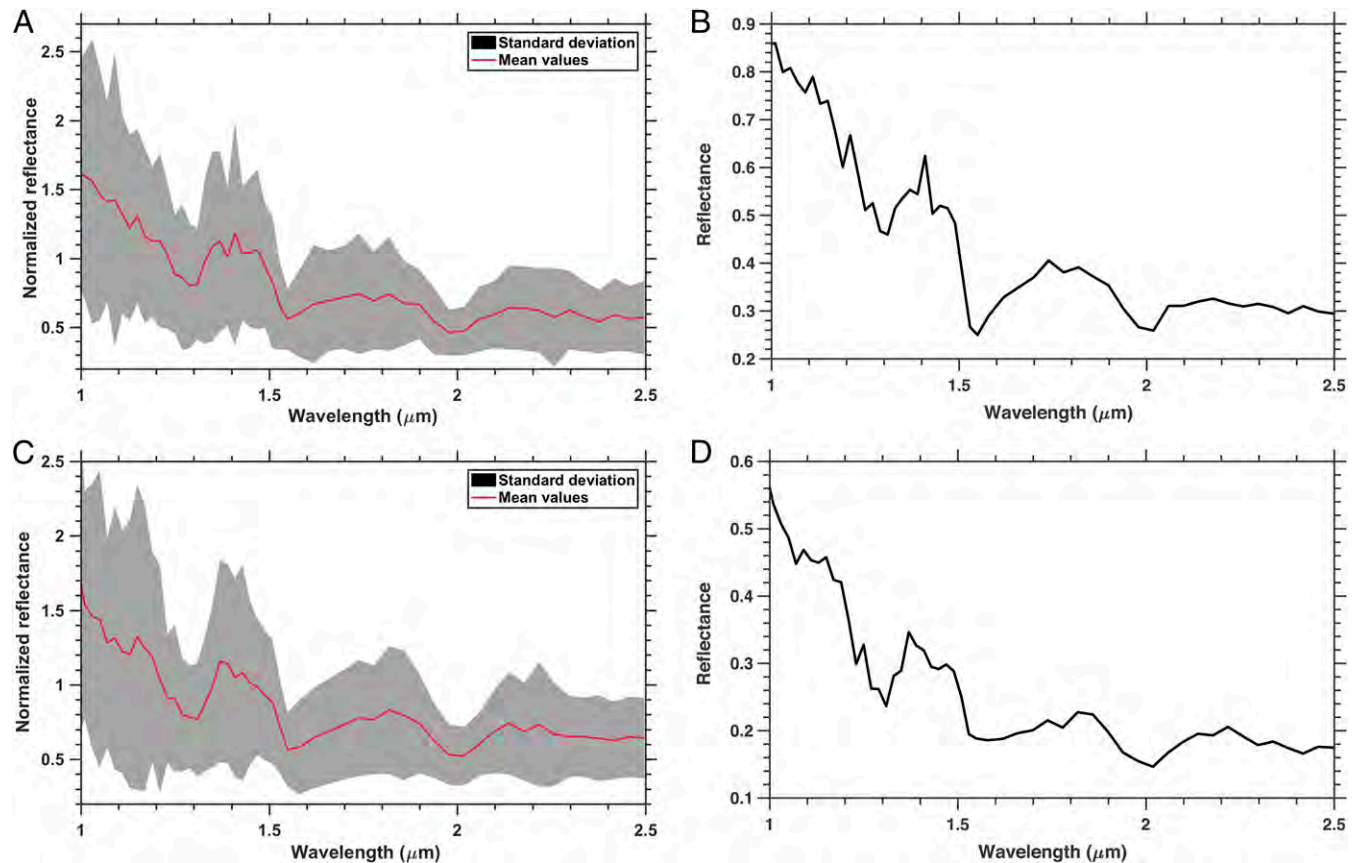


**Fig. 2.** Average spectra and SDs of ice-bearing pixels in the (*A* and *B*) northern and (*C* and *D*) southern polar regions from  $75^\circ$  to  $90^\circ$  latitude. In *A* and *C* we normalized each M (3) spectrum by its mean reflectance for each ice-bearing pixel to accommodate the variation of the intensity of light scattered onto different pixels, which helps to plot the SD of the whole polar region, whereas the average spectra without normalization are shown in *B* and *D*.

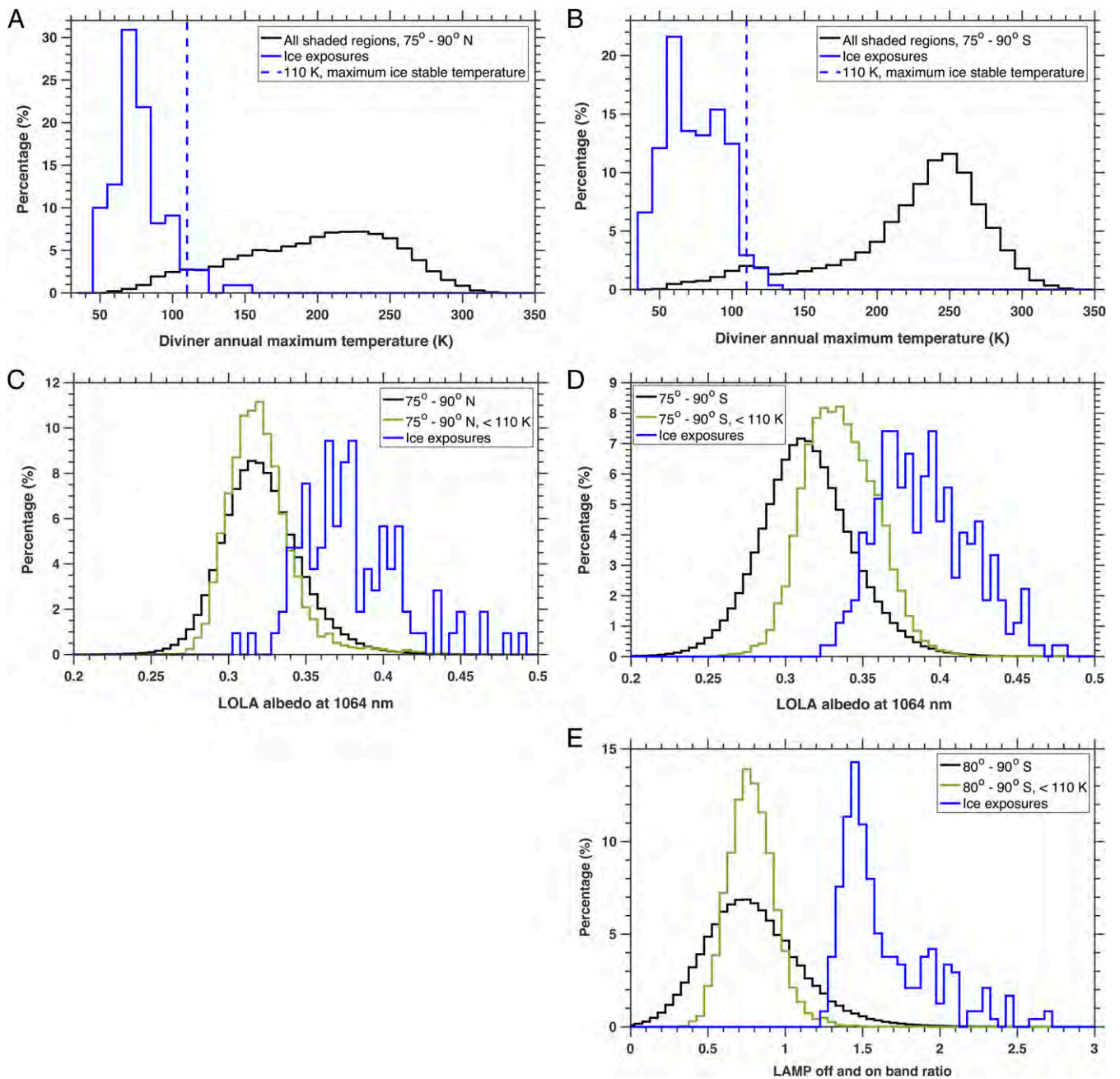


**Fig. 3.** (A) Histogram of maximum surface temperatures for ice-bearing pixels (blue) and all shaded pixels from 75° to 90° latitude (black) in the northern polar region and (B) southern polar region. (C) Histogram of LOLA reflectance values for ice-bearing pixels (blue), surfaces with maximum temperature <110 K (green), and all shaded pixels from 75° to 90° (black) in the northern and (D) southern polar regions (E) LAMP "off" and "on" band ratios for ice-bearing pixels (blue), surfaces with maximum temperature <110 K (green), and all shaded pixels (black); only south polar region LAMP data are available. Each dataset is normalized by the total number of pixels in that dataset.

false detections due to noise in M (3) data. The agreement between these four data sets constitutes a robust detection of water ice at the optical surface in these locations.

The distribution of surface-exposed water ice exhibits strong spatial coherence with temperatures less than 110 K (*SI Appendix, Fig. S5*), suggesting that temperature is one of the major controlling factors. However, not all regions less than 110 K (cold traps) show ice exposures, such as cold traps in craters Amundsen, Hedervari, Idel'son L, and Wiechert near the south pole; the cold trap in Bosch crater and most micro cold traps near 330° longitude between 80° and 85° N near the north pole

(*SI Appendix, Fig. S5*). No bias of M (3) data acquisition occurred at these regions that lack a detection of water ice (*SI Appendix, Fig. S6*). We find that the ice stability depth at these locations is coincidentally greater than zero when the Moon is hypothesized to be on its paleoaxis (*SI Appendix, Fig. S7*) (25), which indicates that surface ice may only be retained at long-timescale cold traps associated with the polar wander, similar to what has been proposed for the dwarf planet Ceres (11).

The patchy distribution and low abundance of surface-exposed water ice in lunar cold traps may reflect a low rate of water supply and a fast rate of regolith gardening process. The Moon is

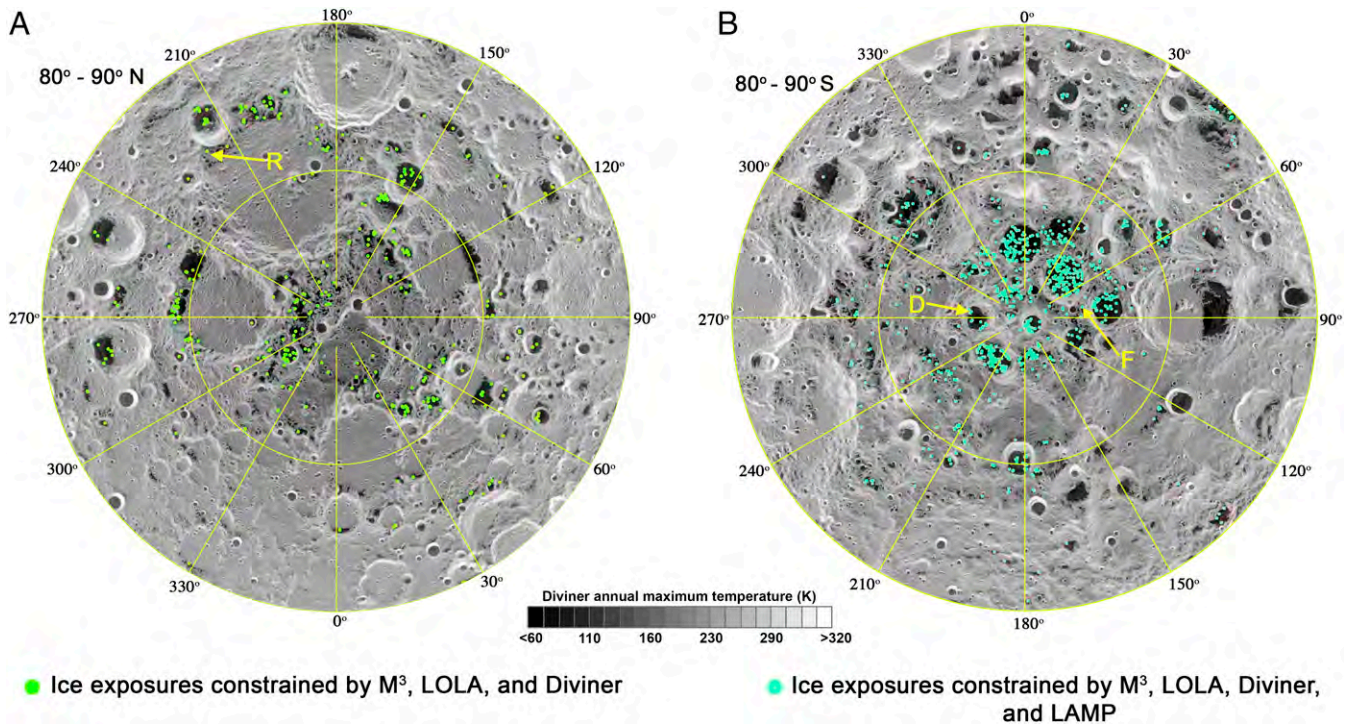


**Fig. 4.** Distribution of water-ice-bearing pixels (green and cyan dots) overlain on the Diviner annual maximum temperature for the (A) northern- and (B) southern polar regions. Ice detection results are further filtered by maximum temperature ( $<110$  K), LOLA albedo ( $>0.35$ ) (12), and LAMP off and on band ratio ( $>1.2$ , only applicable in the south) (13). Each dot represents an M (3) pixel,  $\sim 280$  m  $\times$   $280$  m.

hypothesized to have rotated on its current axis 2–3 Ga ago (25). Since then, no significant amount of ice may have accumulated at newly formed cold traps (i.e., Amundsen, Hedervari, Idel’son, Wiechert, and Bosch), which suggests that the water supply is very slow and the observed ice is very old (older than the time period of polar wander). It is also possible that any new accumulated ice (formed after true polar wander) is thin due to the low rate of supply. Simulations of impact gardening suggest that a layer of frost may last no longer than 20 My on the lunar surface (26). However, it is unclear whether the solar wind bombardment, galactic cosmic rays, and the interplanetary medium UV can cause substantial loss of ice over the geological timescale (2, 27–29). The gardening effect of impacts may mix surface-exposed ice with regolith more efficiently than the accumulation of “new” ice after the proposed true polar wander and result in the observed low ice abundance.

The distribution of locations that meet the criteria for the M (3), LOLA, Diviner, and LAMP (data for southern pole only) data sets (Fig. 4) reveals that the southern polar region exhibits a great number of ice-bearing M (3) pixels than the north because of more shaded regions in the former (*SI Appendix, Fig. S2*). Ice detections in the south are clustered near the craters Haworth, Shoemaker, Sverdrup, and Shackleton, while those in the north are more isolated. Our ice detections near both lunar poles exhibit no bias between the near side and far side (Fig. 4), while the former may have been affected by earthshine, which suggests that our ice detections received negligible or no effects from earthshine. In total, only  $\sim 3.5\%$  of cold traps at both lunar poles exhibit ice signatures, reinforcing the distinction between the Moon and other bodies such as Mercury and Ceres where near-surface ice distribution appears to be controlled primarily by temperature and thus more common in cold traps. In addition, deposits of nearly pure water ice (100% water ice) are inferred for cold traps on Mercury (7, 8) and Ceres (10), whereas the lunar equivalents are suggestive of much lower abundances of ice

( $\sim 30$  wt %). Thus, the delivery, transport, and/or retention of volatiles at the optical surface of the Moon are distinct from other inner solar system objects that have similar cold traps at their poles. Understanding the physical processes responsible for these differences and the timescales on which they operate, including regolith gardening, deposition mechanisms (impact delivery, volcanic outgassing condensation, and water migration), and potential evolution of cold traps due to true polar wander (25), will be a fertile area of future research for understanding volatile behavior in the inner solar system.

## Methods

Potential ice absorption features in surface reflectance spectra near the lunar poles ( $75^\circ$  N/S– $90^\circ$  N/S) were searched for using data acquired by the M (3) (30). The M (3) radiance data acquired during the optical period 2c were downloaded from the Planetary Data System and corrected for thermal contributions using the methods of Li and Milliken (31), although such effects are negligible in shaded regions near the lunar poles. Processed data were binned at a resolution of 128 pixels per degree and then mosaicked from  $75^\circ$  to  $90^\circ$  N/S using a stereographic polar projection and globally using a simple cylindrical projection. Water ice has four diagnostic absorption features centered near 1.1, 1.3, 1.5, and  $2.0\ \mu\text{m}$  at the  $1.0$ – $2.5\text{-}\mu\text{m}$  region (20), the latter three of which were applied as criteria to assess whether M (3) spectra show ice absorption features. In this study we focus on M (3) spectral bands between  $1.0$  and  $2.5\ \mu\text{m}$  due to considerations of signal-to-noise (see *SI Appendix* for detailed justification of using spectral bands at this wavelength range).

The search for ice focused on shadowed areas that were indirectly illuminated by sunlight that had been reflected from nearby, directly illuminated topography. Such reflected light can include spectral reflectance information of the surface material in direct illumination. The true reflectance spectra ( $R_T$ ) in shaded regions can be calculated as

$$R_T = \frac{I}{(J/\pi)R\alpha}, \quad [1]$$

where  $I$  is the radiance captured by the sensor,  $J$  is the solar irradiance spectrum,  $R$  is the bidirectional reflectance at locations where the sunlight is

scattered,  $\alpha$  is the amount of light scattered into the shaded region which depends on the local topography and phase angle and varies from pixel to pixel. The variation of  $\alpha$  will not introduce any absorptions and is only important for quantitative analysis of ice abundance. In this study,  $\alpha$  is set to 1 because we emphasize the global and qualitative assessment of water ice in the lunar polar regions. We assumed  $R$  to be the average reflectance spectra of illuminated regions near the poles (75° N/S–90° N/S) (SI Appendix, Fig. S8). The local solar incidence angle ( $i$ ) was applied as the criterion for determining whether a pixel was shaded ( $i \geq 90^\circ$ ) or illuminated ( $i < 90^\circ$ ). The  $M$  (3) solar incidence angles were derived using a ray-tracing model in conjunction with the LOLA topography data (30) and could be applied to determine shaded or illuminated  $M$  (3) pixels. Shaded pixels identified by this method were also verified by visually checking the  $M$  (3) images.

Radiative transfer modeling results (32) suggest that four diagnostic water-ice absorptions at 1.1, 1.3, 1.5, and 2.0  $\mu\text{m}$  may be detectable in NIR reflectance spectra of intimately mixed ice–regolith mixtures that contain  $>30$  wt % ice, whereas the three longer wavelength (and stronger) absorptions should be observed for ice contents  $>5$  wt % (SI Appendix, Fig. S1). If ice–regolith distribution is spatially heterogeneous and more akin to an areal (checkerboard) mixture at the subpixel scale, then spectral mixing may exhibit linear behavior. In this scenario, linear mixing results indicate that spectra for surfaces with  $>5$  vol % ice should exhibit all four absorptions, whereas the stronger three features would be observable for surfaces with  $>2$  vol % ice (SI Appendix, Fig. S1). The three stronger (longer wavelength) absorptions were used as criteria to examine whether any individual  $M$  (3) spectra showed evidence for water ice, but the centers and widths of these features can vary with particle size (20). The band center and shoulder positions (widths) of ice absorptions for 50–2,000- $\mu\text{m}$  particle sizes were characterized by Clark (20) (SI Appendix, Table S1) and were used as additional criteria to examine  $M$  (3) spectra in shaded regions.

Potential ice-bearing  $M$  (3) pixels were identified in two steps. First, pixels in shaded regions whose spectra exhibited three absorption features matching those in SI Appendix, Table S1 were identified. Cubic spline smoothing (33) was applied to  $M$  (3) spectra to help identify absorption features in this step. Spectral continua of the upper and lower bounds of smoothed  $M$  (3) spectra were calculated, where the former highlight absorption shoulders and the latter define absorption centers. Absorption strength was calculated as the distance between the absorption center point

and the continuum determined by the two shoulder points on either side of the absorption. Although any absorption with an absorption depth greater than zero was considered, only those spectra with absorption center positions and shoulders within the range listed in SI Appendix, Table S3 were counted as possible ice detections.

The second step assessed the spectral angle (SA) between  $M$  (3) pixels identified in step 1 and laboratory spectra of pure water frost. VIS-NIR reflectance spectra of water ice exhibit strong blue continuum slopes (SI Appendix, Fig. S1), a trend that is opposite of typical lunar spectra that exhibit spectral reddening effects due to the presence of nanophase iron formed during space weathering (19). The SA metric can be used to assess the similarity between two spectra, including spectral slopes and absorptions. The spectral angles between individual  $M$  (3) spectra and spectra of pure water frost (Fig. 1) were calculated to assess the similarity of their spectral shapes, defined as

$$SA = \cos^{-1} \left( \frac{|\bar{M} \cdot \bar{I}|}{|\bar{M}| |\bar{I}|} \right), \quad [2]$$

where  $\bar{M}$  is the vector of  $M$  (3) spectra;  $\bar{I}$  is the vector of the spectrum of pure water frost. A 0° spectral angle means that the two vectors are parallel (spectrally similar), whereas a 90° spectral angle means that the two vectors are perpendicular (spectrally dissimilar). We found that spectral angles  $<30^\circ$  may be indicative of the presence of water ice, thus only pixels (spectra) from step 1 with values below this threshold were considered ice-bearing. The 30° threshold was determined by examining the spectral angles of hand-picked ice-bearing and ice-free  $M$  (3) spectra. Original  $M$  (3) spectra of possible ice-bearing pixels that met these criteria were then averaged (without smoothing) for the lunar southern and northern polar regions (75° N/S–90° N/S), respectively.

**ACKNOWLEDGMENTS.** We thank Dr. Roger Clark, Dr. Tim Glotch, and an anonymous reviewer for their fruitful comments. We also thank Dr. Roger Clark for pointing out the shift of the 1.5- $\mu\text{m}$  absorption, which has significantly improved the quality of this paper. We are grateful to Dr. Oded Aharonson for the discussion of the statistical test in this work.

1. Urey HC (1952) *The Planets: Their Origin and Development* (Yale Univ Press, New Haven, CT).
2. Arnold JR (1979) Ice in the lunar polar regions. *J Geophys Res* 84:5659–5668.
3. Watson K, Murray BC, Brown H (1961) The behavior of volatiles on the lunar surface. *J Geophys Res* 66:3033–3045.
4. Vasavada AR, Paige DA, Wood SE (1999) Near-surface temperatures on mercury and the moon and the stability of polar ice deposits. *Icarus* 141:179–193.
5. Salvail JR, Fanale FP (1994) Near-surface ice on mercury and the moon—A topographic thermal-model. *Icarus* 111:441–455.
6. Ingersoll AP, Svitek T, Murray BC (1992) Stability of polar frosts in spherical bowl-shaped craters on the Moon, Mercury, and Mars. *Icarus* 100:40–47.
7. Neumann GA, et al. (2013) Bright and dark polar deposits on Mercury: Evidence for surface volatiles. *Science* 339:296–300.
8. Paige DA, et al. (2013) Thermal stability of volatiles in the north polar region of Mercury. *Science* 339:300–303.
9. Deutsch AN, Neumann GA, Head JW (2017) New evidence for surface water ice in small-scale cold traps and in three large craters at the north polar region of Mercury from the Mercury Laser Altimeter. *Geophys Res Lett* 44:9233–9241.
10. Platz T, et al. (2016) Surface water-ice deposits in the northern shadowed regions of Ceres. *Nat Astron* 1:0007.
11. Schorghofer N, et al. (2017) The putative Cerean exosphere. *Astrophys J* 850:85.
12. Fisher EA, et al. (2017) Evidence for surface water ice in the lunar polar regions using reflectance measurements from the Lunar Orbiter Laser Altimeter and temperature measurements from the Diviner Lunar Radiometer Experiment. *Icarus* 292:74–85.
13. Hayne PO, et al. (2015) Evidence for exposed water ice in the Moon's south polar regions from Lunar Reconnaissance Orbiter ultraviolet albedo and temperature measurements. *Icarus* 255:58–69.
14. Lawrence D, et al. (2011) Sensitivity of orbital neutron measurements to the thickness and abundance of surficial lunar water. *J Geophys Res Planets* 116:E01002.
15. Hibbitts CA, Stockstill-Cahill K, Takir D (2017) Ultraviolet reflectance spectroscopy measurements of carbonaceous meteorites and planetary analog materials. Available at [adsabs.harvard.edu/abs/2017DPS...4941710H](https://adsabs.harvard.edu/abs/2017DPS...4941710H). Accessed August 6, 2018.
16. Zuber MT, et al. (2012) Constraints on the volatile distribution within Shackleton crater at the lunar south pole. *Nature* 486:378–381.
17. Pieters CM, et al. (2009) Character and spatial distribution of OH/H<sub>2</sub>O on the surface of the Moon seen by M3 on Chandrayaan-1. *Science* 326:568–572.
18. Li S, Milliken RE (2017) Water on the surface of the Moon as seen by the Moon Mineralogy Mapper: Distribution, abundance, and origins. *Sci Adv* 3:e1701471.
19. Pieters C, Fischer E, Rode O, Basu A (1993) Optical effects of space weathering: The role of the finest fraction. *J Geophys Res Planets* 98:20817–20824.
20. Clark RN (1981) Water frost and ice—The near-infrared spectral reflectance 0.65–2.5  $\mu\text{m}$ . *J Geophys Res* 86:3087–3096.
21. Libowitzky E (1999) Correlation of OH stretching frequencies and OH...O hydrogen bond lengths in minerals. *Monatsh Chem/Chem Mon* 130:1047–1059.
22. Poch O, et al. (2016) Sublimation of water ice mixed with silicates and tholins: Evolution of surface texture and reflectance spectra, with implications for comets. *Icarus* 267:154–173.
23. Schriver-Mazzuoli L, Schriver A, Hallou A (2000) IR reflection-absorption spectra of thin water ice films between 10 and 160 K at low pressure. *J Mol Struct* 554:289–300.
24. Williams JP, Paige DA, Greenhagen BT, Sefton-Nash E (2017) The global surface temperatures of the moon as measured by the diviner lunar radiometer experiment. *Icarus* 283:300–325.
25. Siegler MA, et al. (2016) Lunar true polar wander inferred from polar hydrogen. *Nature* 531:480–484.
26. Hurlley DM, et al. (2012) Two-dimensional distribution of volatiles in the lunar regolith from space weathering simulations. *Geophys Res Lett* 39:L09203.
27. Crites ST, Lucey PG, Lawrence DJ (2013) Proton flux and radiation dose from galactic cosmic rays in the lunar regolith and implications for organic synthesis at the poles of the Moon and Mercury. *Icarus* 226:1192–1200.
28. Gladstone GR, et al. (2012) Far-ultraviolet reflectance properties of the Moon's permanently shadowed regions. *J Geophys Res Planet* 117:E00H04.
29. Lanzerotti LJ, Brown WL, Poate J, Augustyniak W (1978) Low energy cosmic ray erosion of ice grains in interplanetary and interstellar media. *Nature* 272:431–433.
30. Green R, et al. (2011) The Moon Mineralogy Mapper (M3) imaging spectrometer for lunar science: Instrument description, calibration, on-orbit measurements, science data calibration and on-orbit validation. *J Geophys Res Planets* 116:E00G19.
31. Li S, Milliken RE (2016) An empirical thermal correction model for Moon Mineralogy Mapper data constrained by laboratory spectra and Diviner temperatures. *J Geophys Res Planets* 121:2081–2107.
32. Hapke B (1981) Bidirectional reflectance spectroscopy: I. Theory. *J Geophys Res* 86:3039–3054.
33. de Boor C (1978) *A Practical Guide to Splines* (Springer, New York), pp 207–240.